IOP Publishing Superconductor Science and Technology
Supercond. Sci. Technol. 31 (2018) 065001 (10pp) https://doi.org/10.1088/1361-6668/aab93d

Superconductivity in palladium-doped 2H-TaS_2

M H Zhou[1,2], X C Li[1,2] and C Dong[1,3]

[1] Institute of Physics, Chinese Academy of Sciences, Beijing 100190, People's Republic of China
[2] University of Chinese Academy of Sciences, Beijing 100049, People's Republic of China

E-mail: chengdon@aphy.iphy.ac.cn

Received 29 January 2018, revised 20 March 2018
Accepted for publication 23 March 2018
Published 25 April 2018

Abstract

A series of Pd_xTaS_2 ($0.01 \leqslant x \leqslant 0.08$) samples were prepared and characterized via scanning electron microscope, x-ray powder diffraction, resistivity, magnetization and specific heat measurements. The lattice parameter c associated with the interlayer distance increases monotonically with the Pd content while the parameter a remains essentially constant. The crystal structure of $Pd_{0.08}TaS_2$ has been determined and refined by Rietveld refinement. $Pd_{0.08}TaS_2$ is hexagonal (space group: P31c) with lattice parameters $a = 3.3151(1)$ Å, $c = 12.1497(9)$ Å. The superconducting transition temperature T_c (0.8 K) of TaS_2 can be dramatically enhanced by Pd doping, and the maximum T_c of 4.2 K, about five times the T_c of pure TaS_2, is obtained in $Pd_{0.04}TaS_2$. We have determined the superconducting parameters of $Pd_{0.04}TaS_2$, and found that the enhancement of T_c can be attributed to the increase of density of states at the Fermi level. The charge density wave (CDW) of TaS_2 is gradually suppressed with Pd doping and disappears in $Pd_{0.06}TaS_2$. This suggests that there is a competitive interplay between superconductivity and CDW in this system.

Keywords: superconductivity, palladium-doped, 2H-TaS_2, charge density wave

(Some figures may appear in colour only in the online journal)

1. Introduction

Layered transition metal dichalcogenides (TMDs) have unusual electronic, mechanical and optical properties [1, 2]. Metal atoms and organic molecules can be easily intercalated into the interlayers and hence tune their properties [3–9]. TaS_2 is a layered dichalcogenide that has several polytypes, for example, 1 T, 2 H and $4H_b$ types [10–12]. 1T-TaS_2 is a semiconductor with a commensurate charge density wave (CDW) phase below 180 K [13–15]. Tuned by pressure, the superconductivity of 1T-TaS_2 develops within the commensurate CDW state and survives to very high pressure [13]. 2H-TaS_2 is a metal with CDW ($T_{CDW} = 75$ K) [16] and superconductivity ($T_c = 0.8$ K) [17]. The superconductivity of 2H-TaS_2 has been enhanced by alkali metal Na [18], 3*d* transition metals [19, 20] and organic molecules [21, 22]. The Na-intercalated 2H-TaS_2 has a maximum T_c of 4.4 K [18]. The CDW weakens with Na doping, as observed from resistivity and optical measurements [18, 23]. The raise of T_c in Na_xTaS_2 may be caused by the increase of density of states at the Fermi level $N(E_F)$. Both Ni- [19] and Cu-doping [20] can obviously suppress the CDW transition and enhance the superconductivity of 2H-TaS_2. 2H-Ni_xTaS_2 ($0 \leqslant x \leqslant 0.08$) and 2H-$Cu_xTaS_2$ ($0 \leqslant x \leqslant 0.12$) were found to have the maximum T_c of 4.15 K and 4.5 K, respectively. Gamble *et al* [21] reported some superconducting organic intercalation complexes of 2H-TaS_2. The transition temperature varies between 1.5 and 4.5 K, and increases generally with the number of molecules per TaS_2. The enhancement of superconductivity in this system results from the increase of density of states.

According to prior reports [18–20], the reason for enhancement of superconductivity and the interplay between superconductivity and CDW in doped 2H-TaS_2 are not clear. We propose to further explore the possible origins of these phenomena in 2H-TaS_2 system by doping. In this paper, we first report the effects of 4*d* transition metal Pd doping on both superconductivity and CDW of 2H-TaS_2. Pd is chosen because it is nonmagnetic, with electron configuration $4d^{10}$; moreover, recently Pd doping has induced superconductivity

[3] Author to whom any correspondence should be addressed.

 © 2018 IOP Publishing Ltd Printed in the UK

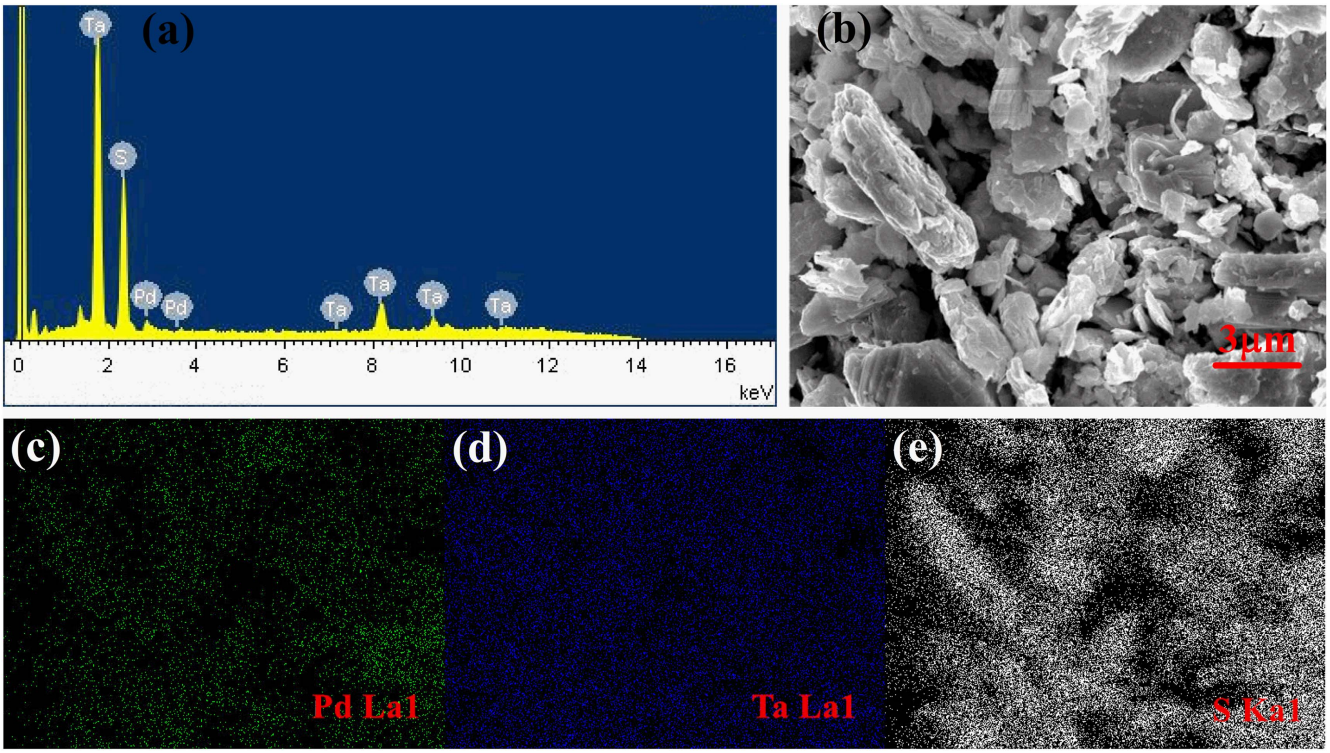

Figure 1. (a) EDX spectrum of $Pd_{0.04}TaS_2$. (b) SEM image of $Pd_{0.04}TaS_2$. (c)–(e) Elemental mappings of $Pd_{0.04}TaS_2$ for the area in (b).

in $TiSe_2$ [24] and enhanced superconductivity of $TaSe_2$ [25]. The superconductivity and CDW of Pd_xTaS_2 system were studied by resistivity, magnetization and specific heat measurements. In addition, the prior reports [20, 24, 25] simply considered that the intercalated atoms locate at the octahedral interstices in intercalated TMDs, while the actual crystal structure of intercalated TMDs had not been determined. The crystal structure of Pd_xTaS_2 was determined and refined by the Rietveld method in this work.

2. Experimental

The polycrystalline samples of Pd_xTaS_2 ($0.01 \leqslant x \leqslant 0.08$) were prepared by the solid-state reaction method. Stoichiometric amounts of Pd (99.99%, Sinopharm Chemical Reagent, Co., Ltd, China), Ta (99.9%, Aladdin) and S (99.5%, Alfa Aesar) powders were fully mixed, and then pressed into pellets, sealed in evacuated quartz tubes. The first heating cycle was performed at 923 K for 2 d. Samples were air quenched to room temperature and then ground, pressed into pellets which were resealed in evacuated quartz tubes. The samples were heated at 1023 K for 2 d and then annealed at 923 K for two weeks, and finally air quenched to room temperature.

A scanning electron micrograph, energy dispersive x-ray (EDX) spectroscopy and x-ray elemental mapping were acquired on a Hitachi S-4800 field-emission scanning electron microscope. Powder x-ray diffraction data were collected using a Rigaku Ultima-IV x-ray diffractometer with CuK_α radiation. The lattice parameters were refined with the PowderX software [26]. The crystal structure was refined with the Rietveld method (FullProf package [27]). Magnetization measurements were performed using a vibrating sample magnetometer (Quantum Design, MPMS-VSM). The electrical resistivity was measured by the standard four-probe method in a physical property measurement system (Quantum Design, PPMS-9). The heat capacity measurements were taken in the same PPMS by the thermal relaxation method.

3. Results and discussion

To verify the homogeneity of the Pd_xTaS_2 samples, we acquired the EDX spectrum and elemental mapping of the representative sample ($Pd_{0.04}TaS_2$), as shown in figure 1. The EDX spectrum (figure 1(a)) shows characteristic peaks of Pd around 2.8 and 3.6 keV. The content of Pd obtained from the EDX spectrum is about 0.038, close to the nominal one. The elemental mappings (figures 1(c)–(e)) for the area in figure 1(b) indicate that Pd is evenly distributed in $Pd_{0.04}TaS_2$. Thus, both EDX spectrum and elemental mapping confirm that the sample has high homogeneity.

We studied the crystal structure of Pd_xTaS_2 ($0.01 \leqslant x \leqslant 0.08$) samples via x-ray diffraction and crystal structure refinement. Powder x-ray diffraction patterns of these samples are shown in figure 2(a). The major phase (Pd_xTaS_2) can be indexed with a hexagonal cell. The slight amount of impurity is Ta_2O_5. The lattice parameters of the Pd_xTaS_2 were refined by a least-square method, and the results are shown in figure 2(b). As the content of Pd increases, the *c*-axis parameter increases monotonically from 12.097 Å ($x = 0.01$) to 12.147 Å ($x = 0.08$), while the *a*-axis parameter remains

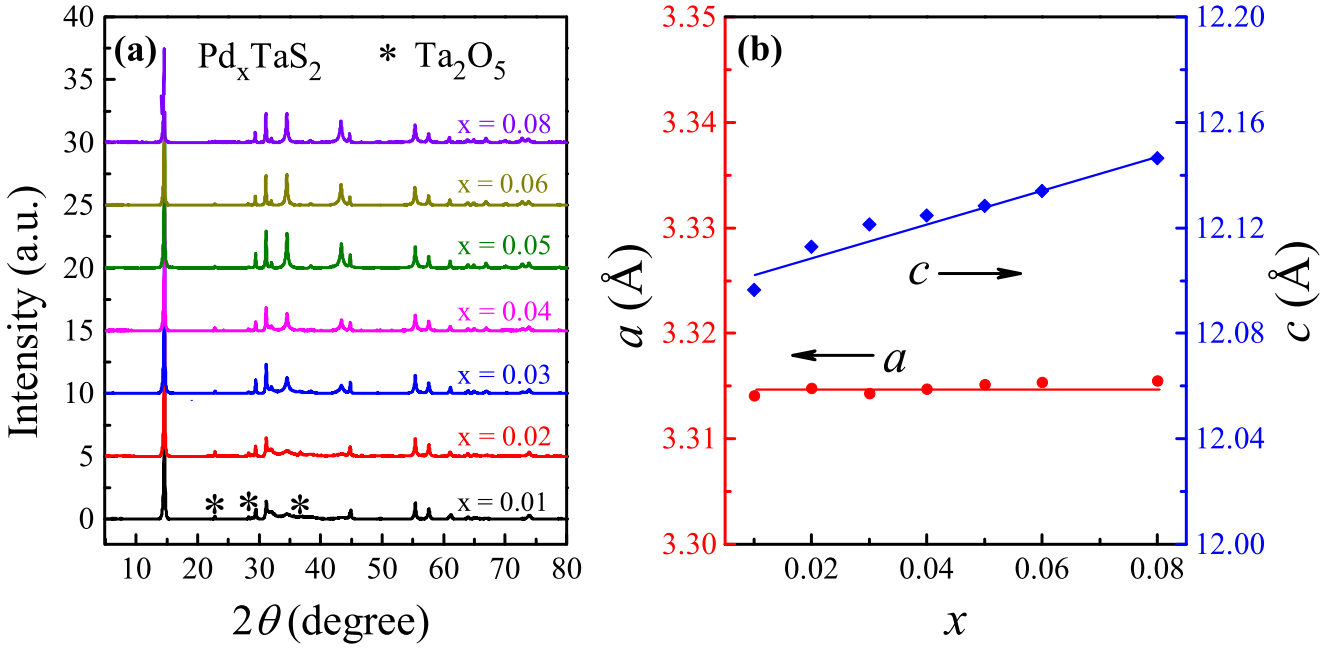

Figure 2. (a) Powder x-ray diffraction patterns for Pd_xTaS_2 ($0.01 \leqslant x \leqslant 0.08$) samples. The peaks of impurity Ta_2O_5 are marked by asterisks. (b) Variation of the lattice parameters with Pd content x in Pd_xTaS_2. The solid lines in (b) are guides to the eye.

Table 1. Crystallographic data and Rietveld refinement results for $Pd_{0.08}TaS_2$ at room temperature.

Space group			P31c (No. 159)		
$a = b = 3.3151(1)$ Å, $c = 12.1497(9)$ Å, $V = 115.641$ Å^3, $Z = 2$					
$R_p = 9.14\%$, $R_{wp} = 9.98\%$, $R_B = 3.06\%$, $R_F = 1.65\%$, $R_{exp} = 1.60\%$					
Atom	Site	x	y	z	Occ
Pd	2*a*	0	0	0.50	0.093
Ta	2*a*	0	0	0.2076	1
S1	2*b*	1/3	2/3	0.5767	1
S2	2*b*	2/3	1/3	0.3245	1
Bond length (Å)			Bond angle (°)		
Ta-S1		2.488	S1-Ta-S1		83.534
Ta-S2		2.383	S2-Ta-S2		88.131

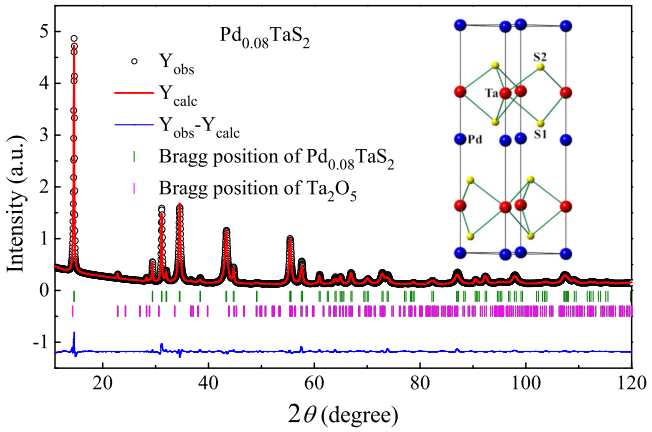

Figure 3. Rietveld refinement profile for $Pd_{0.08}TaS_2$ sample. Vertical bars (|) indicate the positions of the Bragg peaks. The bottom trace depicts the difference between the observed and calculated intensity values. The inset shows the schematic of crystal structure for $Pd_{0.08}TaS_2$.

almost unchanged (3.315 Å). The variation of the lattice parameters indicates that Pd intercalates into the interlayers of the TaS_2 lattice.

Putting Pd atoms at the octahedral interstices, we have tried different structure models using possible space group (space group $P6_3/mmc$ and its subgroups) to fit the diffraction data of all Pd_xTaS_2 ($0.01 \leqslant x \leqslant 0.08$) samples, and found the best fit can be obtained by adopting space group P31c. The obtained structure model is applicable to all Pd_xTaS_2 samples. Due to the structure distortion with Pd intercalation, the crystal symmetry of Pd_xTaS_2 (space group P31c) is lower than that of pure 2H-TaS_2 (space group $P6_3/mmc$) [28]. Rietveld refinements were performed using the FullProf software package [27]. The refined crystallographic data and the R factors for $Pd_{0.08}TaS_2$ are summarized in table 1. Final agreement factors converged to $R_B = 3.06\%$ and $R_{wp} = 9.98\%$. The good fit between the observed and calculated plots suggests that the crystal structure model is correct. The Rietveld refinement profile and the schematic of crystal structure are shown in figure 3. As shown in the inset of figure 3, the S-Ta-S shows trigonal-prism coordination. The Pd atoms occupy the octahedral interstices in the interlayer of TaS_2, and each Pd atom is surrounded by six S atoms to form a slightly distorted PdS_6 octahedron.

The superconductivity of Pd_xTaS_2 ($0.01 \leqslant x \leqslant 0.08$) has been investigated via resistivity, magnetization and specific heat measurements. The temperature dependence of normalized resistivity of Pd_xTaS_2 samples are shown in figure 4(a). With increasing of Pd content, the residual resistivity ratio

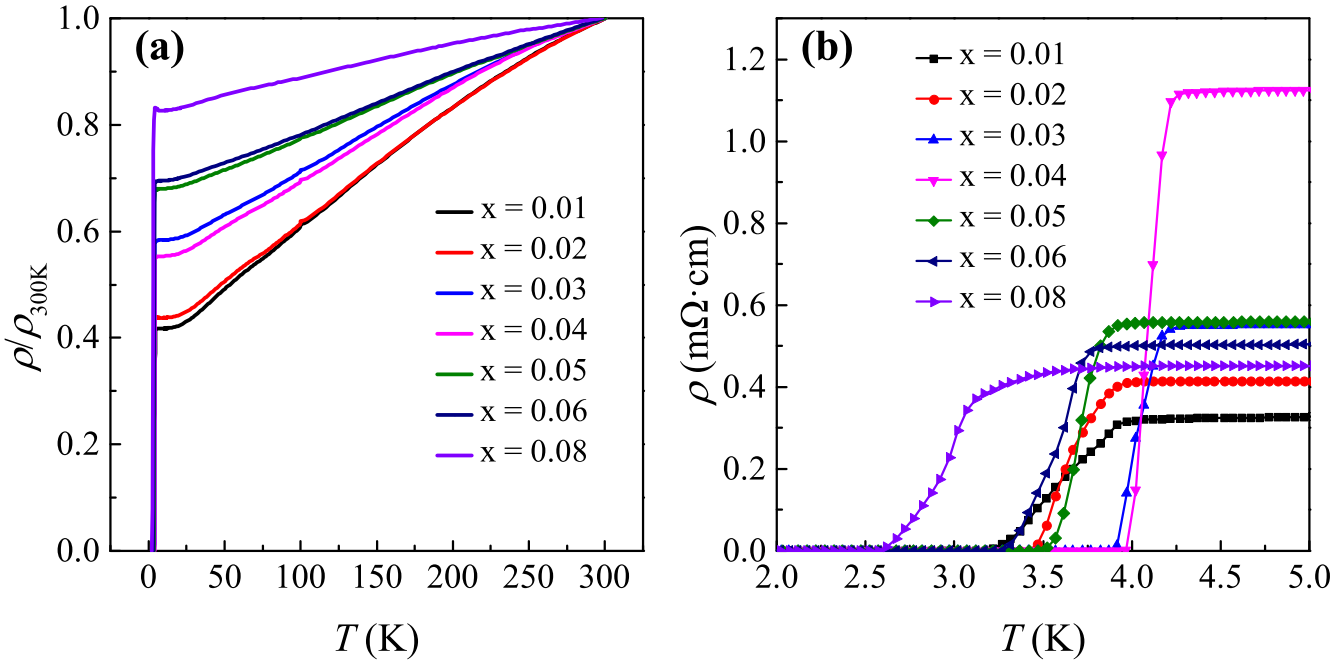

Figure 4. (a) Temperature dependence of normalized resistivity for Pd_xTaS_2 ($0.01 \leqslant x \leqslant 0.08$) samples. (b) Detail of superconducting transitions in Pd_xTaS_2 ($0.01 \leqslant x \leqslant 0.08$).

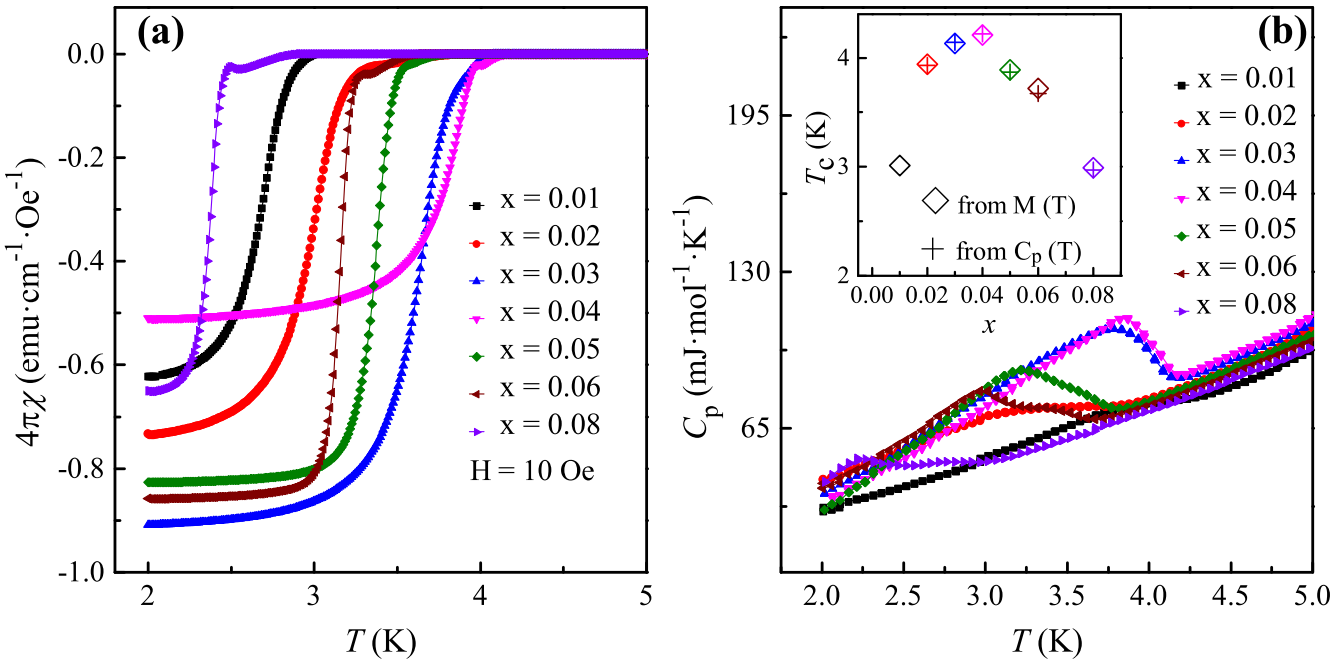

Figure 5. (a) Temperature dependence of magnetization for Pd_xTaS_2 ($0.01 \leqslant x \leqslant 0.08$) under zero field cooling in an applied magnetic field $H = 10$ Oe. (b) Temperature dependence of specific heat for Pd_xTaS_2 ($0.01 \leqslant x \leqslant 0.08$). The inset shows the T_c-x phase diagram determined from magnetization and specific heat measurements.

(RRR) decreases systematically, suggesting that the intercalated compounds thus evolve into bad metals. The scattering between the conducting carriers and the foreign atoms may be the origin of the observed evolution of RRR [29]. All samples exhibited superconducting transitions at low temperature. Figure 4(b) shows detail of the transitions for all samples, presenting the increase and then decrease in T_c with Pd doping. The maximum T_c of about 4.2 K for $Pd_{0.04}TaS_2$ was observed in the resistivity measurement. A sharp transition with width less than 0.5 K for $Pd_{0.04}TaS_2$ again confirms the high homogeneity of the superconducting phase.

Figure 5(a) shows the temperature dependence of magnetization for Pd_xTaS_2 samples under zero field cooling in an applied field of 10 Oe. The low-field magnetizations indicate the presence of bulk superconductivity in this system. The T_c first increases to around 4.2 K for $Pd_{0.04}TaS_2$ and then

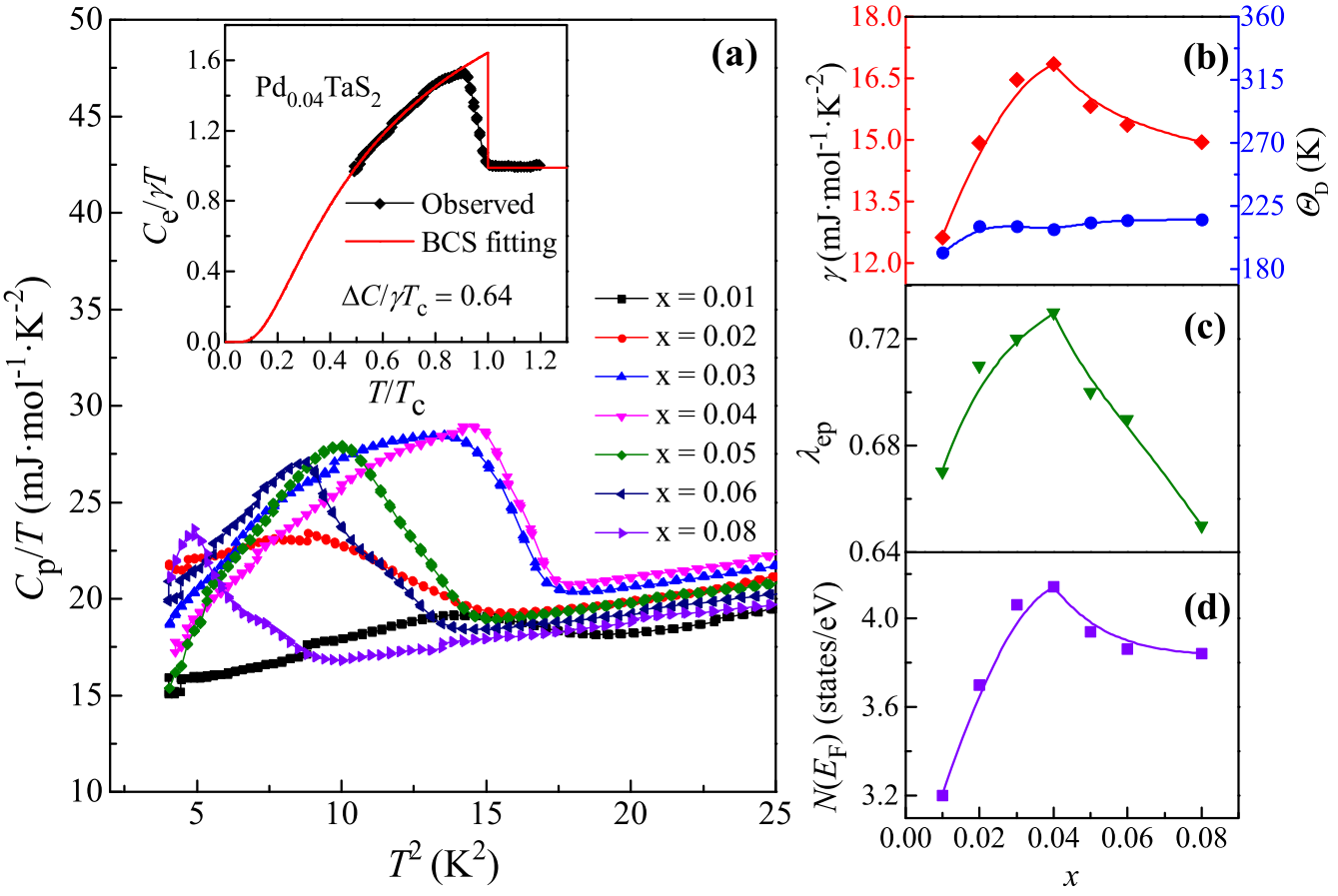

Figure 6. (a) The C/T versus T^2 curves for Pd_xTaS_2 ($0.01 \leqslant x \leqslant 0.08$) samples. The inset shows the electronic specific heat contribution for $Pd_{0.04}TaS_2$ near the superconducting transition. The red solid line in the inset is the BCS fitting curve. (b) Variations of γ and Θ_D with Pd content x in Pd_xTaS_2 system. Variations of (c) λ_{ep} and (d) $N(E_F)$ with Pd content x in Pd_xTaS_2 system. The solid lines in (b)–(d) are guides to the eye.

Table 2. T_c, γ, Θ_D, $N(E_F)$ and λ_{ep} in various TMDs.

Compound	T_c (K)	γ (mJ mol^{-1} K^{-2})	Θ_D (K)	λ_{ep}	$N(E_F)$ (states/eV)	References
$Pd_{0.04}TaS_2$	4.2	16.84	208.5	0.73	4.14	This work
2H-TaS_2	0.8	8	165	0.52[a]	2.23[a]	[20]
2H-$Cu_{0.04}TaS_2$	4.5	12	165	0.8[a]	2.8[a]	[20]
2H-$Ni_{0.04}TaS_2$	4.15	13.02	244.7[a]	0.688[a]	3.27[a]	[19]
2H-$TaSe_2$	0.14	5	202	0.4	1.51	[25]
2H-$Pd_{0.09}TaSe_2$	3.3	8.5	196	0.67	2.16	[25]
2H-$Ni_{0.02}TaSe_2$	2.79	8.13	196.8	0.653	2.09	[31]
2H-$Cu_{0.07}TaSe_2$	2.7	8.56	178.8	0.657	2.2	[32]
1T-$Cu_{0.08}TiSe_2$	4.1	4.3	162.8[a]	0.78[a]	1.02[a]	[33]
1T-$Pd_{0.12}TiSe_2$	2	3.25	166.9[a]	0.63[a]	0.85[a]	[24]

[a] Denote the calculated parameters based on the data in [19, 20, 24] and [33]. 2H structure (space group: $P6_3/mmc$) and 1 T structure (space group: P-3m1). $Pd_{0.04}TaS_2$ has a distorted 2H structure (space group: P31c).

decreases to about 2.9 K for $Pd_{0.08}TaS_2$. The evolution of T_c with Pd content is consistent with that observed in resistivity measurement. It is obvious that as little as 1% Pd intercalation pushes the T_c of 2H-TaS_2 up by a factor of around 4.0—from 0.8 to about 3.0 K.

The low-temperature specific heat of Pd_xTaS_2 samples are shown in figure 5(b). C–T curves for all samples show clear peaks at the superconducting transitions, giving another evidence for bulk superconductivity. The inset of figure 5(b) shows the superconducting transition temperatures obtained by specific heat and magnetization measurements as functions of Pd content x, and they are accurately consistent. It is obvious that the T_c-x phase diagram exhibits a dome-like behavior. The maximum T_c of 4.2 K is observed in $Pd_{0.04}TaS_2$. The maximum T_c of this system is significantly higher than that of Pd_xTiSe_2 (2.0 K) [24] and Pd_xTaSe_2 (3.3 K) [25] system.

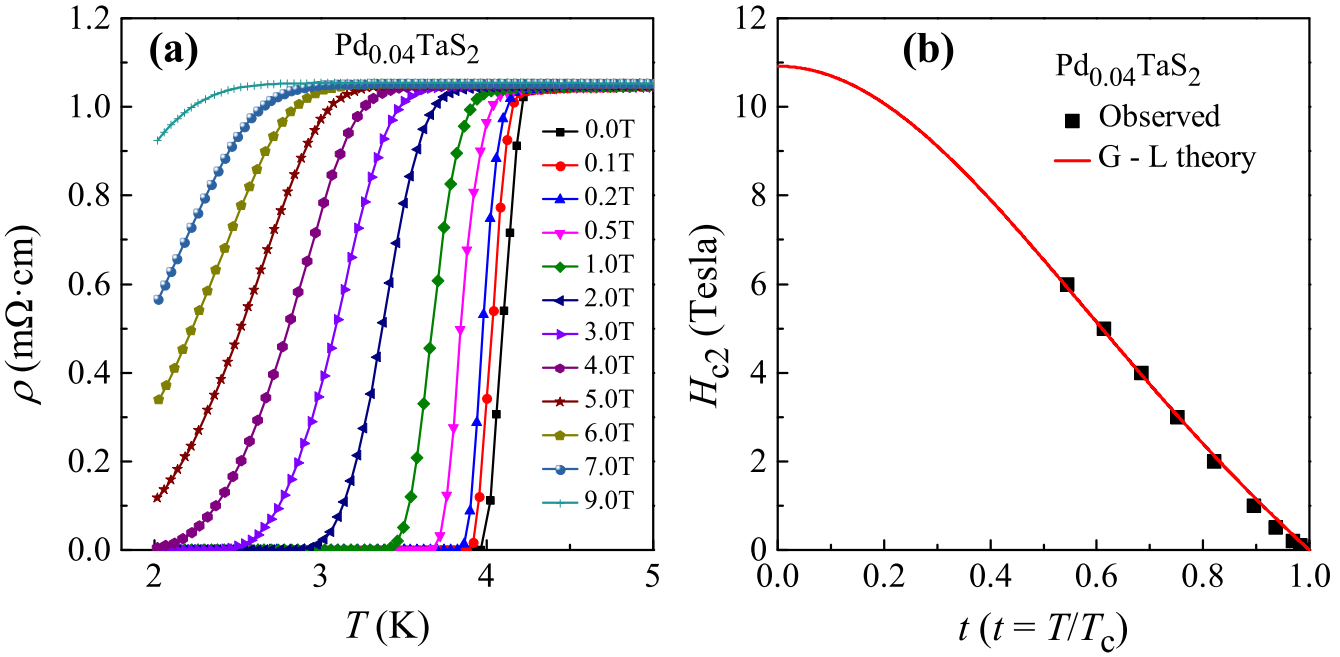

Figure 7. (a) Temperature dependence of resistivity for $Pd_{0.04}TaS_2$ measured in various applied magnetic fields. (b) Temperature dependence of upper critical field H_{c2} for $Pd_{0.04}TaS_2$. The red solid line in (b) shows the fitted curve by the Ginzberg–Landau theory.

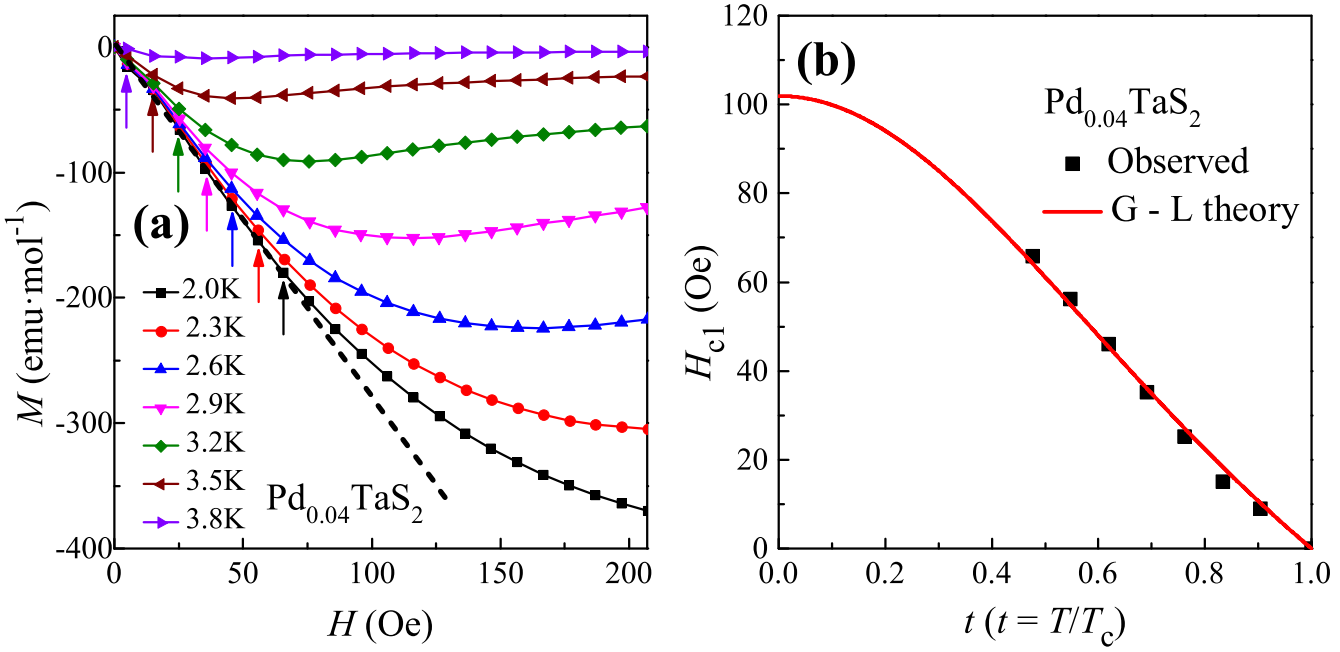

Figure 8. (a) Field dependence of magnetization at different temperatures for $Pd_{0.04}TaS_2$. The fields where the M–H curves deviate from linearity are marked by colored arrows. (b) Temperature dependence of lower critical field H_{c1} for $Pd_{0.04}TaS_2$. The red solid line in (b) shows the fitted curve by the Ginzberg–Landau theory.

The C/T versus T^2 curves for Pd_xTaS_2 samples are shown in figure 6(a). The normal state specific heat are well described as a sum of the T-linear electronic contribution and the T^3 phonon contribution, such that $C/T = \gamma + \beta T^2$ [20], where γ and β are electronic and phonon specific heat coefficient, respectively. The Debye temperature Θ_D is calculated using the formula $\Theta_D = [(n \times 1.944 \times 10^6)/\beta]^{1/3}$ [19], where n is the number of atoms per formula unit. The values of Θ_D for all samples are shown in figure 6(b). It is apparent that the Θ_D remains almost unchanged as $x > 0.02$ ($\Theta_D \approx 210$ K). Figure 6(b) also shows the evolution of γ with Pd content. The γ first increases to a maximum value of 16.84 mJ mol^{-1} K^{-2} in $Pd_{0.04}TaS_2$ and then decreases to 14.94 mJ mol^{-1} K^{-2} in $Pd_{0.08}TaS_2$. The electron–phonon

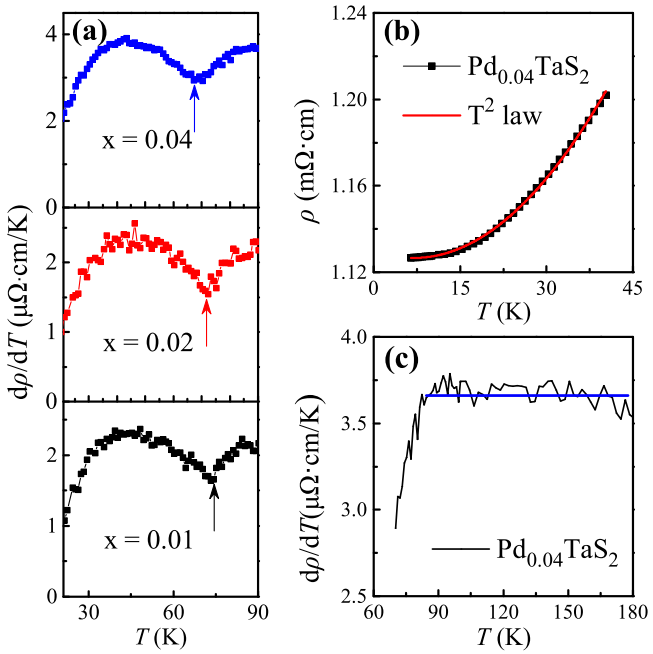

Figure 9. (a) ($d\rho/dT$) versus T curves for Pd_xTaS_2 ($x = 0.01$, 0.02 and 0.04). (b) Temperature dependence of normal-state resistivity for $Pd_{0.04}TaS_2$ with temperature below 40 K. The red solid line in (b) shows the fitted curve by the T^2 law. (c) ($d\rho/dT$) versus T curve for $Pd_{0.04}TaS_2$ with temperature ranging from T_{CDW} to 180 K. The blue solid line in (c) is a guide for the eye.

coupling parameter λ_{ep} can be calculated with the inverted McMillan formula [30]:

$$\lambda ep = \frac{1.04 + \mu^* \ln\left(\frac{\Theta_D}{1.45T_c}\right)}{(1-0.62\mu^*)\ln\left(\frac{\Theta_D}{1.45T_c}\right) - 1.04} \quad (1)$$

where the Coulomb pseudopotential parameter μ^* is taken as 0.15. The calculated results are shown in figure 6(c). The values of λ_{ep} are less than the minimum value 1.0 of strong coupling, implying that the Pd_xTaS_2 is an intermediate or weak coupling superconductor. The inset in figure 6(a) shows the electronic specific heat C_e for $Pd_{0.04}TaS_2$ near the superconducting transition with phonon contribution subtracted. With the isotropic single-gap BCS model, the electronic specific heat jump at T_c, $\Delta C/\gamma T_c$, is estimated to be about 0.64, significantly deviating from the ideal BCS ratio of 1.43.

The superconductivity in the TMDs is generally considered to be of the conventional BCS type [18]. According to BCS theory, T_c rises as Θ_D and N (E_F) increase. In Pd_xTaS_2 system, the Θ_D remains essentially constant, suggesting that the N (E_F) plays a major role in the evolution of T_c. The N (E_F) can be calculated from the equation N (E_F) $= 3\gamma/[\pi^2 k_B{}^2(1 + \lambda_{ep})]$ [25]. The calculated N (E_F) values for all samples are plotted in figure 6(d). The evolution of N (E_F) with Pd content x is consistent with that of T_c with x. Thus, the evolution of superconductivity in this system is essentially controlled by the variation of N (E_F). The Pd intercalation induces the increase of partial Pd density of state by hybridization with the TaS_2 states near the Fermi level, which may contribute to the variation of N (E_F) in Pd_xTaS_2.

We compared the T_c, γ, Θ_D, $N(E_F)$ and λ_{ep} of $Pd_{0.04}TaS_2$ with those of other superconducting TMDs (table 2) and analyzed the effect of N (E_F) on T_c from the perspective of structural types. We found that the N (E_F) is indeed a key factor in determining T_c magnitude for doped TMDs of the same structural type. Nevertheless, for those of different structural types, the cases are complicated. For instance, $Pd_{0.04}TaS_2$ (with a distorted 2H structure), 2H-$Cu_{0.04}TaS_2$ and 1T-$Cu_{0.08}TiSe_2$ with almost the same λ_{ep}, having nearly identical T_c values but notably different N (E_F) values. The microscopic mechanism of the enhancement of T_c in TMDs remains unclear, and hence further theoretical and experimental studies are essential.

In order to determine the upper critical field, we measured the temperature dependence of resistivity at different applied magnetic fields for $Pd_{0.04}TaS_2$ (figure 7(a)). It is noticed that the resistive transitions shift parallel down to lower temperature with the increase of magnetic field. Figure 7(b) presents the upper critical field H_{c2} as a function of temperature determined from the mid-point of the transition curves. The H_{c2} can be well fitted by the Ginzberg–Landau equation H_{c2} $(T) = H_{c2}$ (0) $[(1 - t^2)/(1 + t^2)]$, where $t = T/T_c$ is the reduced temperature, H_{c2} (0) is the zero temperature upper critical field. By fitting, H_{c2} (0) is estimated to be about 10.9 T. It is known that $H_{c2} = \Phi_0/2\pi\xi^2$ with Φ_0 being the flux quanta and ξ being the coherence length. ξ (0) is estimated to be about 5.50 nm.

Figure 8(a) shows the M–H curves of $Pd_{0.04}TaS_2$ in the low-field region at different temperatures. At low fields, the M–H isotherm is linear in H, as expected for a BCS type-II superconductor. The lower critical field H_{c1} values at different temperatures are estimated from the points where the M–H curves deviate from linearity. As shown in figure 8(b), the H_{c1} also can be fitted by the Ginzberg–Landau equation. The H_{c1} (0) is estimated to be about 102 Oe. From the relation $H_{c1} = (\Phi_0/4\pi\lambda^2)\ln(\lambda/\xi)$, we obtain the zero temperature penetration depth λ $(0) = 248$ nm. The Ginzburg–Landau parameter κ $(0) = \lambda$ $(0)/\xi$ (0) is estimated to be of the order of 45, confirming type-II superconductivity in this sample.

The CDW of Pd_xTaS_2 system has been studied by resistivity and magnetization measurements. It is found that the resistivity ρ decreases smoothly with temperature and no apparent sign of CDW transition is observed on the normalized resistivity curve (figure 4(a)). Nevertheless, the CDW transition can be identified from the valley of the $d\rho/dT$ curve (figure 9(a)). It is obvious that T_{CDW} decreases as Pd doping increases. As shown in figure 9(b), for $Pd_{0.04}TaS_2$, the normal-state resistivity ρ (T) below 40 K obeys a T^2 law, being consistent with the Fermi liquid behavior. The other samples show similar behavior to that of $Pd_{0.04}TaS_2$. It is interesting to note that ρ increases quite linearly with temperature ranging from roughly above T_{CDW} to about 180 K as evidenced in figure 4(a). To verify this linear behavior, we show the $d\rho/dT$ curve of this temperature range for $Pd_{0.04}TaS_2$ (figure 9(c)). The constant slope marked by a blue solid line clarifies the above observation. The linear behavior within a wide range

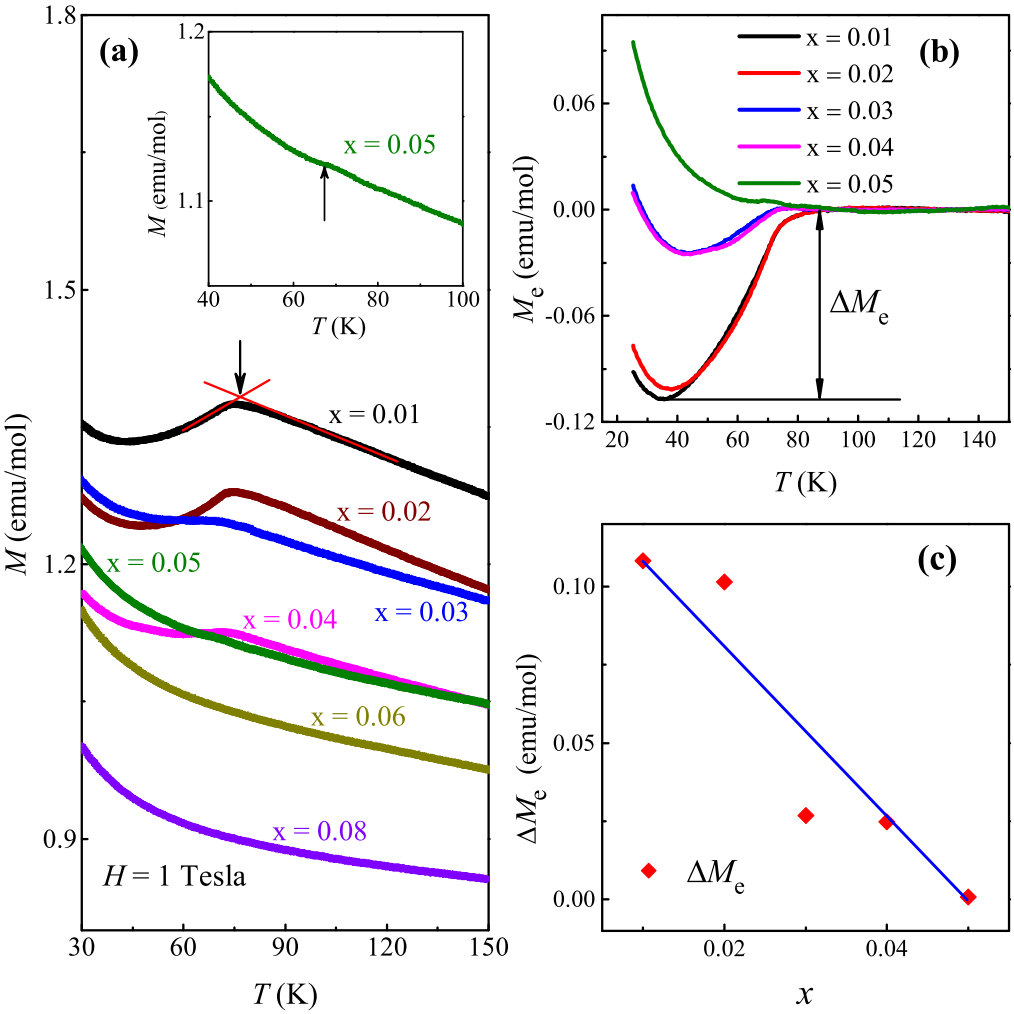

Figure 10. (a) Temperature dependence of normal state magnetization of Pd_xTaS_2 ($0.01 \leqslant x \leqslant 0.08$) under an applied field $H = 1$ T. The red solid lines in (a) are guides to the eye. (b) Temperature dependence of electronic magnetization M_e of Pd_xTaS_2 ($0.01 \leqslant x \leqslant 0.05$). ΔM_e is determined as the difference between the magnetization value of the start point of transition and the minimum magnetization value on the M_e–T curve. (c) ΔM_e as a function of Pd content x. The blue solid line in (c) is a guide for the eye.

could be attributed to the formation of pseudogap above T_{CDW} [25, 34, 35]. The decrease of $d\rho/dT$ near T_{CDW} in figure 9(c) indicates the decrease of the number of the conducting electrons due to the formation of the CDW gap.

Figure 10(a) shows the high-field ($H = 1$ T) magnetization in normal state for Pd_xTaS_2 samples. T_{CDW} could be determined from the onset of the magnetization drop as shown by arrows in figure 10(a). It is in good agreement with the T_{CDW} observed in resistivity measurement. The T_{CDW} decreases as the Pd content increases. The M–T curve with temperature above T_{CDW} shows a paramagnetic behavior and can be well fitted by Curie–Weiss law. The magnetization M can be separated into two terms: the first one is the Curie–Weiss term come from the contribution of paramagnetic ions, the second one is the electronic term M_e, proportional to the density of states at Fermi level, i.e. $M_e \propto N(E_F)$. M_e can be obtained by subtracting the Curie–Weiss term from the total magnetization, as shown in figure 10(b). The formation of CDW results in the reduction of $N(E_F)$, so M_e decreases (see figure 10(b)). We introduce ΔM_e as a measure of the strength of the CDW. The ΔM_e as a function of Pd content x is shown in figure 10(c). The ΔM_e decreases when the Pd content increases, indicating that the CDW is gradually suppressed by the Pd doping. The disruption of the CDW order is responsible for the broadening of the transition peak. A Curie–Weiss-like tail appears in the low temperature, possibly due to a small local moment induced by Pd intercalation [25]. The CDW transition remains in $Pd_{0.05}TaS_2$ (see the inset of figure 10(a)), but it could not be identified in the $M(T)$ curves for $x \geqslant 0.06$, indicating that the CDW is completely suppressed at high doping levels.

According to the above analysis, we give an electronic phase diagram for Pd_xTaS_2 ($0.01 \leqslant x \leqslant 0.08$) system in figure 11. The T_c first increases and then decreases with Pd doping, namely, exhibiting a dome behavior. The increase of $N(E_F)$ and the strengthen of the electron–phonon coupling are mainly responsible for the increase of T_c. The T_{CDW} decreases with increasing Pd content and the CDW is not observed for $x \geqslant 0.06$. The strength of CDW transition simultaneously weakens as Pd doping increases (see figure 10). We calculated

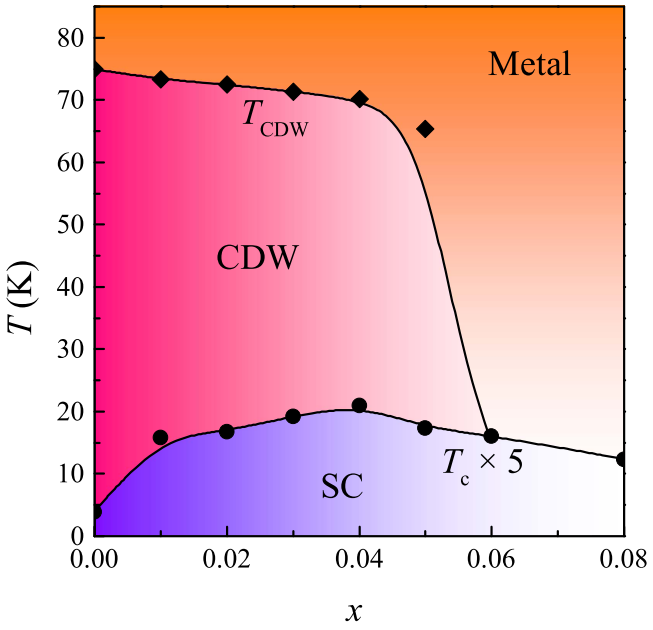

Figure 11. Electronic phase diagram for Pd_xTaS_2 ($0.01 \leqslant x \leqslant 0.08$) system. The solid lines are guides to the eye.

the bond length (Ta–S: 2.467 Å) of pristine 2H-TaS_2 (space group: $P6_3/mmc$) from the data in [36]. The bond lengths of $Pd_{0.08}TaS_2$ (space group: P31c) are 2.488 Å (Ta-S1) and 2.383 Å (Ta-S2). By comparing the crystal symmetry and the bond lengths of $Pd_{0.08}TaS_2$ with those of 2H-TaS_2, we found that there is a remarkable structure distortion in Pd intercalated TaS_2. The structure distortion disrupts the coherence of the CDW and hence shrinks the CDW domain size. This may be the major factor in suppressing the CDW state in this system. From the perspective of electronic phase separation [13], in TMDs with both superconductivity and CDW order, the electrons near the Fermi level can be separated into two parts: one part supports the superconductivity, whereas another part contributes to the formation of CDW phase. The destruction of the ordering of the CDW state results in the redistribution of the electrons near the Fermi level. This also plays an important role in enhancing the T_c. Overall, the superconductivity is enhanced progressively with Pd content up to the optimal doping level, while the CDW is gradually suppressed. This implies that there is a competition between superconductivity and CDW in this system. Beyond the optimal doping level, the superconductivity slowly weakens, nevertheless, the CDW vanishes quickly, likewise confirming the above-mentioned competitive relation.

4. Conclusions

A series of Pd_xTaS_2 ($0.01 \leqslant x \leqslant 0.08$) samples were prepared and characterized by x-ray diffraction, resistivity, magnetization and specific heat measurements. The crystal structure of $Pd_{0.08}TaS_2$ has been determined and refined by Rietveld refinement. $Pd_{0.08}TaS_2$ is hexagonal (space group: P31c) with lattice parameters $a = 3.3151(1)$ Å, $c = 12.1497(9)$ Å. The superconducting transition temperature of TaS_2 can be dramatically enhanced by Pd doping, and optimal doped $Pd_{0.04}TaS_2$ has a T_c of 4.2 K. The evolution of superconductivity in this system is mainly attributed to the variation of $N(E_F)$. The electronic phase diagram was derived for the Pd_xTaS_2 system. CDW is suppressed with Pd doping and disappears in $Pd_{0.06}TaS_2$, revealing the competitive relationship between superconductivity and CDW in this system. The origin of the enhancement of T_c and the interplay between superconductivity and CDW in TMDs remain open questions, our work provides valuable information for further understanding the physics in these superconductors.

Acknowledgments

This work was supported by the National Natural Science Foundation of China (Grant No. 21271183).

ORCID iDs

M H Zhou https://orcid.org/0000-0002-1503-7055
X C Li https://orcid.org/0000-0002-1270-4828

References

[1] Neto A H C 2001 *Phys. Rev. Lett.* **86** 4382–5
[2] Klemm R A 2015 *Physica* C **514** 86–94
[3] Friend R H and Yoffe A D 1987 *Adv. Phys.* **36** 1–94
[4] Gamble F R, Di Salvo F J, Klemm R A and Geballe T H 1970 *Science* **168** 568–70
[5] Murphy D W, Di Salvo F J, Hull G W and Waszczak J V 1976 *Inorg. Chem.* **15** 17–21
[6] Schlicht A, Lerf A and Biberacher W 1999 *Synth. Met.* **102** 1483–4
[7] Fleming R M and Coleman R V 1975 *Phys. Rev. Lett.* **34** 1502–5
[8] Meyer S F, Howard R E, Stewart G R, Acrivos J V and Geballe T H 1975 *J. Chem. Phys.* **62** 4411–9
[9] Lerf A, Sernetz F, Biberacher W and Schöllhorn R 1979 *Mater. Res. Bull.* **14** 797–805
[10] Hayashi K and Kawamura A 1986 *Mater. Res. Bull.* **21** 1405–10
[11] Jellinek F 1962 *J. Less-Common Met.* **4** 9–15
[12] Di Salvo F J, Bagley B G, Voorhoeve J M and Waszczak J V 1973 *J. Phys. Chem. Solids.* **34** 1357–62
[13] Sipos B, Kusmartseva A F, Akrap A, Berger H, Forró L and Tutiš E 2008 *Nat. Mater.* **7** 960–5
[14] Thompson A H, Gamble R F and Revelli J F 1971 *Solid State Commun.* **9** 981–5
[15] Fazekas P and Tosatti E 1979 *Phil. Mag.* B **39** 229–44
[16] Tonjes W C, Greanya V A, Liu R, Olson C G and Molinié P 2001 *Phys. Rev.* B **63** 235101
[17] Smith T F, Shelton R N and Schwall R E 1975 *J. Phys. F: Met. Phys.* **5** 1713–25
[18] Fang L, Wang Y, Zou P Y, Tang L, Xu Z, Chen H, Dong C, Shan L and Wen H H 2005 *Phys. Rev.* B **72** 014534
[19] Li L J, Zhu X D, Sun Y P, Lei H C, Wang B S, Zhang S B, Zhu X B, Yang Z R and Song W H 2010 *Physica* C **470** 313–7
[20] Wagner K E *et al* 2008 *Phys. Rev.* B **78** 104520
[21] Gamble F R, Osiecki J H and DiSalvo F J 1971 *J. Chem. Phys.* **55** 3525–30

[22] Meyer S F, Acrivos J V and Geballe T H 1975 *Proc. Natl Acad. Sci.* **72** 464–8
[23] Hu W Z, Li G, Yan J, Wen H H, Wu G, Chen X H and Wang N L 2007 *Phys. Rev.* B **76** 045103
[24] Morosan E, Wagner K E, Zhao L L, Hor Y, Williams A J, Tao J, Zhu Y and Cava R J 2010 *Phys. Rev.* B **81** 094524
[25] Bhoi D, Khim S, Nam W, Lee B S, Kim C, Jeon B G, Min B H, Park S and Kim K H 2016 *Sci. Rep.* **6** 24068
[26] Dong C 1999 *J. Appl. Cryst.* **32** 838
[27] Rodríguez-Carvajal J 1993 *Physica* B **192** 55–69
[28] Mattheiss L F 1973 *Phys. Rev.* B **8** 3719–40
[29] Zhu X D, Sun Y P, Zhang S B, Lei H C, Li L J, Zhu X B, Yang Z R, Song W H and Dai J M 2009 *Solid State Commun.* **149** 1296–9
[30] McMillan W L 1968 *Phys. Rev.* **167** 331–44
[31] Li L J, Sun Y P, Zhu X D, Wang B S, Zhu X B, Yang Z R and Song W H 2010 *Solid State Commun.* **150** 2248–52
[32] Li X C, Zhou M H, Yang L H and Dong C 2017 *Supercond. Sci. Technol.* **30** 125001
[33] Morosan E, Zandbergen H W, Dennis B S, Bos J W G, Onose Y, Klimczuk T, Ramirez A P, Ong N P and Cava R J 2006 *Nat. Phys.* **2** 544–50
[34] Vescoli V, Degiorgi L, Berger H and Forró L 1998 *Phys. Rev. Lett.* **81** 453–6
[35] Ruzicka B, Degiorgi L, Berger H, Gaál R and Forró L 2001 *Phys. Rev. Lett.* **86** 4136–9
[36] Meetsma A, Wiegers G A, Haange R J and De Boer J L 1990 *Acta Cryst.* C **46** 1598–9